Statistical comparison of various dayside magnetopause reconnection X-line prediction models

Ramiz A. Qudsi[1,*], Brian Walsh[1], Jeff Broll[2], Emil Atz[1], Stein Haaland[3]

[1]Center for Space Physics, Boston University
[2]Los Alamos National Lab
[3]The University Center in Svalbard, Longyearbyen, Norway

Key Points:

- Compared four different reconnection line models.
- On average, the Maximum Bisection Field Model gives the best prediction of reconnection line location.
- The Maximum Exhaust Velocity model gives the worst prediction of the reconnection line location.

Corresponding author: Ramiz Qudsi, `qudsira@bu.edu`

Abstract

Reconnection at Earth's magnetopause drives magnetospheric convection and provides mass and energy input into the magnetosphere/ionosphere system thereby driving the coupling between solar wind and terrestrial magnetosphere. Despite its importance, the factors governing the location of dayside magnetopause reconnection are not well understood. Though a few models can predict X-line locations reasonably well, the underlying physics is still unresolved. In this study we present results from a comparative analysis of 274 magnetic reconnection events as observed by the Magnetospheric Multiscale (MMS) mission to determine what quantities affect the accuracy of such models and are most strongly associated with the occurrence of dayside magnetopause reconnection. We also attempt to determine under what upstream solar wind conditions each global X-line model becomes least reliable.

Plain Language Summary

Magnetic reconnection is an energy transferring process that happens at the Earth's magnetopause, the boundary between Earth's local plasma environment and the Sun's interplanetary environment. Reconnection helps move energy and particles into the region of space surrounding the earth called the magnetosphere. Dayside reconnection is important because it is a defining element to the amount of energy deposited into our magnetosphere, and state of safety to human life on Earth. Despite its importance, scientists still do not completely understand how it works and where it happens. This study looks at many observations of magnetic reconnection to try and understand its precise location and figure out under which conditions it is more likely to occur. This paper compares in-situ data with different models for predicting reconnection locations.

1 Introduction

The interplanetary magnetic field (IMF) emanating from the sun interacts with the terrestrial magnetic field giving rise to a complex and rich structures of scientifically interesting phenomena. The interaction between these two fields result in a reorientation of the topology of the magnetic field lines. This process is known as magnetic reconnection. The process is accompanied by the conversion of energy and is the primary process for exchange of particles between the solar wind and the magnetosphere (e.g., Paschmann, 2008). In three dimensional space, the location of reconnection is a line known as X-line. Magnetic reconnection at Earth's magnetopause deposits energy into the terrestrial magnetic field, the results of which have important consequences for the shape, size, and dynamics of the magnetosphere.

In the classical picture of magnetic reconnection, ignoring the Earth's dipole tilt, reconnection occurs at the sub-solar point when Earth's magnetic field lines encounter southward IMF, and in the polar cusp region for the northward IMF (Dungey, 1961). Southward IMF at the sub-solar point, the point of the magnetosphere closest to the sun, results in a process called anti-parallel reconnection since the Earth's magnetic field is in the Northward direction. On the other hand, for an arbitrary direction and magnitude of IMF, the location of reconnection is more complicated (Paschmann, 2008; Paschmann et al., 2013). Component reconnection occurs when the two reconnecting magnetic fields have some components of their directions perpendicular to the reconnection plane. Using in-situ spacecraft data as well as simulation data, both anti-parallel and component reconnection have been shown to occur at the magnetopause (Crooker, 1979; Gonzalez & Mozer, 1974; Paschmann et al., 2013, 2018, 1986; Fuselier et al., 2011; Trattner et al., 2007).

The location of reconnection sites, or X-lines, is crucial for understanding the dynamics of the magnetosphere and the effects of space weather at Earth. To predict the

Table 1. A list of reconnection models, the parameters which are maximized and the name given to those models in this study.

Model No.	Reference	Parameter	Name
1	Moore (2002)	Reconnecting component	Maximum Bisection Field Model
2	Trattner et al. (2007)	Magnetic shear	Maximum Shear Model
3	Cassak and Shay (2007)	Hybrid Alfvén velocity	Maximum Exhaust Velocity Model
4	Hesse et al. (2013)	Reconnection energy	Maximum Reconnection Energy Model

location of an X-line at the dayside magnetopause, multiple models have been developed over the last few decades. Some of these models encompass features of both anti-parallel and component reconnection. A sub-set of these models suggest that reconnection occurs along a line or in a region where some physical quantity or a parameter is maximized. Table 1 lists four models compared in this study and the parameter which is maximized in each of the models. The fourth column lists the name of the corresponding model as has been used in this study.

One assumption in each of these models is that reconnection occurs as a single spatially extended X-line across the dayside magnetopause. Inherent in each of these models is a prediction for what underlying physics controls the location of reconnection at the interface between the shocked solar wind and magnetosphere. None of them have been rigorously tested against other models using simulation or in-situ data. Komar et al. (2015) compared, among others, the models listed in Table 1 using global resistive magnetohydrodynamic (MHD) simulations and largely concluded that:

1. For the chosen [MHD] simulation parameters, we [Komar et. al. (2015)] find that all models are within a few Earth radii (R_{E}) of the magnetic separators when the IMF has a southward orientation and no dipole tilt.
2. None of the models chosen for this study faithfully reproduce the entire magnetic separators when the IMF has a northward orientation and no dipole tilt. However, only the maximum magnetic shear model faithfully reproduces the portion of the separator nightward of the magnetic nulls where reconnection is expected to occur.

For all the tested models, results were within a few Earth radii of the magnetic separators when the IMF had a southward orientation, but only the maximum magnetic shear model faithfully reproduced the portion of the separator nightward of the magnetic nulls when the IMF had a northward orientation. Komar et al. (2015) did not directly compare the models' outputs, nor was a statistical study done. Souza et al. (2017) compared the output from three different analytical models (Maximum Shear Model, Maximum Current Density Model and Maximum Exhaust Velocity Model) with different spacecraft data. However, the study was done only for two reconnection events and thus lacked statistical significance. Nevertheless, several studies have validated the output of the Maximum Shear Model from different data sets (e.g., Petrinec et al., 2022; Trattner et al., 2021; Fuselier et al., 2017; Trattner, Burch, et al., 2017; Trattner, Thresher, et al., 2017). Another study was done recently by Liu et al. (2018) using a three dimensional particle-in-cell simulations in which they compared the results to different rate model predictions.

Among the models that Liu et al. (2018) compared their predictions with, they found that for X-line orientation, the Maximum Reconnection Energy Model provided the closest predictions.

Given the use of some of these models for mission designing and answering science questions (Fuselier et al., 2014), it is thus important to conduct a comparative study of these models using in-situ spacecraft data for varying upstream solar wind conditions. In this study we thus present a statistical comparison between four different dayside magnetopause reconnection X-line prediction models. The next section (Section 2) introduces and gives a brief overview of the four different X-line prediction models (listed in Table 1) considered in this study. Section 3 discusses all the data, both observation and simulation, used in this study as well as describes the methodology in detail. In the following section (Section 4) we present the results from the study and discuss the performance of the models for varying upstream solar wind conditions. Finally, Section 5 summarizes and concludes the study.

2 Science Background

There are several models in the literature that predict the location of the dayside magnetopause reconnection X-line. In this study we consider four such models (see Table 1) all of which have a common feature, they maximize a parameter along the magnetopause to find the location of X-line. In this section, a brief overview of each model is presented to provide the necessary scientific background.

2.1 Maximum Shear Model

The Maximum Shear Model is an empirical model for the location of a reconnection X-line along the magnetopause surface based on the ion-flux distribution in the high-altitude cusps (Trattner et al., 2007). The model posits that reconnection "occurs along a ridge of maximum magnetic shear between the opposing magnetic fields on the two sides of the magnetopause" (Trattner et al., 2021). In order to find the location of the X-line, the maximum of the shear angle between the two opposing fields is found which is given as:

$$\cos(\theta) = \left(\mathbf{B}_{\mathrm{sh}} \cdot \mathbf{B}_{\mathrm{msp}}\right) / \left(|\mathbf{B}_{\mathrm{sh}}||\mathbf{B}_{\mathrm{msp}}|\right) \tag{1}$$

where, $\mathbf{B}_*$ is the magnetic field and 'sh' and 'msp' refers to the magnetosheath and magnetosphere respectively. Sections 3.1 and 3.2 describe in detail how the relevant data for each side is obtained.

Though the original Maximum Shear Model study only considered southward IMF conditions (Trattner et al., 2007), a more recent study has shown the model to be valid for northward IMF conditions as well without losing statistical accuracy as long as B_{y} is the dominant component ($B_{\mathrm{y}}/|\mathbf{B}| > 0.8$) (Trattner, Thresher, et al., 2017). Since its inception, several studies in literature have quantified the performance of Maximum Shear Model (Trattner, Burch, et al., 2017; Fuselier et al., 2017; Komar et al., 2015).

2.2 Maximum Reconnection Energy

The Maximum Reconnection Energy Model is a theoretical model proposed by Hesse et al. (2013) to describe the collisionless magnetic reconnection of asymmetric systems. The model suggests that in an asymmetric system, the magnetic reconnection line is oriented in such a way that the product of available magnetic energy is maximized. For magnetosphere and solar wind magnetic interactions the following parameter is maximized:

$$E \propto \left(|\mathbf{B}_{\text{sh}}|^2 \times |\mathbf{B}_{\text{msp}}|^2 \right) \tag{2}$$

where E is proportional to the available energy from two available fields. The model was originally proposed and supported by small scale reconnection simulations and has been tested using a MHD simulation. Komar et al. (2015) compared several dayside magnetic reconnection models in global magnetosphere simulations, one of which was Maximum Reconnection Energy Model and found that Maximum Reconnection Energy Model was within a few Earth radii (R_{E}) of X-line for southward IMF and no dipole tilt. The model is strictly two dimensional and to enhance confidence in the model, a full three dimensional treatment of the theory is required.

2.3 Maximum Exhaust Velocity

The Maximum Exhaust Velocity Model is an application of a model proposed by Cassak and Shay (2007). The model conjectures that the X-line orientation is determined by maximizing the asymmetric reconnection outflow speed which is described as:

$$V_{\text{A}} \sim \left[\frac{B_{\text{sh}} B_{\text{msp}} \left(B_{\text{sh}} + B_{\text{msp}} \right)}{\left(n_{\text{i,msp}} B_{\text{sh}} + n_{\text{i,sh}} B_{\text{msp}} \right)} \right]^{1/2} \tag{3}$$

where $n_{\text{i,msp}}$ and $n_{\text{i,sh}}$ refers to the ion density in magnetosphere and magnetosheath respectively. The predictions of this model have been found to be consistent with spacecraft observations of reconnection poleward of the cusp (Muzamil et al., 2014) as well as observations in simulation (Cassak & Fuselier, 2016; Komar et al., 2015). One of the limitations of the model is that it ignores the importance of plasma velocity parallel to the direction of reconnecting magnetic field (Komar et al., 2015).

2.4 Maximum Bisection Field

The Maximum Bisection Field Model was proposed by Moore (2002) to predict the location of the dayside X-line along the locus of points where the two opposite field lines, magnetospheric and magnetosheath, are bisected. This simplifies to finding the location where the following field is maximized:

$$B_{\text{rec}} = |\mathbf{B}_{\text{msp}} \cdot \mathbf{i}_{\text{xn}}| \tag{4}$$

where, B_{rec} is the field component to be maximized and $\mathbf{i}$ is the the unit vector normal to the x-line. If the slope of the reconnection line were `m`, then the slope of the unit vector $\mathbf{i}_{\text{xn}}$ will be `-1/m`. Once the location of maximum reconnecting field is found, the X-line is then found by integrating away from the point along the bisector of angle between the local fields. One of the assumption of Moore (2002) is that bisection only leads to equal and opposite reconnecting components if the magnitude of the magnetic field on both sides of the current sheet is the same, however this is not always the case for a full 3-D fields.

For the 2-D case, this direction is identical to the direction along which the proportional available magnetic energy is maximized as given by the Maximum Reconnection Energy Model (Hesse et al., 2013). This means that maximizing either Equation (2) or Equation (4) should give identical results. However, as seen in Section 4, for a full 3-D case, though the output from two models look very similar (see right panels in Figure 4), the location of the X-line as computed by maximizing each of the two parameters give slightly different results (see Tables 3 and 4).

Figure 1 shows the distribution of each of the four parameters discussed in this section, projected on the yz-plane. The parameters have been normalized against their respective maximum values. The three rows correspond to three different IMF conditions

(shown at the top right of each plot). Top row corresponds to a purely southward IMF whereas the bottom row corresponds to purely northward IMF. Middle row shows the distribution for Parker spiral like condition with zero field in z-direction. Clock angle for each IMF is shown in top left corner. For these sample plots, the ion density (n_p) is assumed to be $5\,\mathrm{cm}^{-3}$ with plasma bulk velocity of -500 km/s in the x-direction and an average ion temperature of 1.5×10^{-6} K. The DST index is -5 nT and the dynamic pressure is 2.4 nPa. For simplicity, Earth's dipole tilt was assumed to be zero for all three cases. The magnetic fields were computed using the Tsyganenko-96 model (Tsyganenko, 1996). See Section 3.2 for more details on how these images were generated. These figures are similar to those reported in literature (Moore, 2002; Trattner et al., 2007).
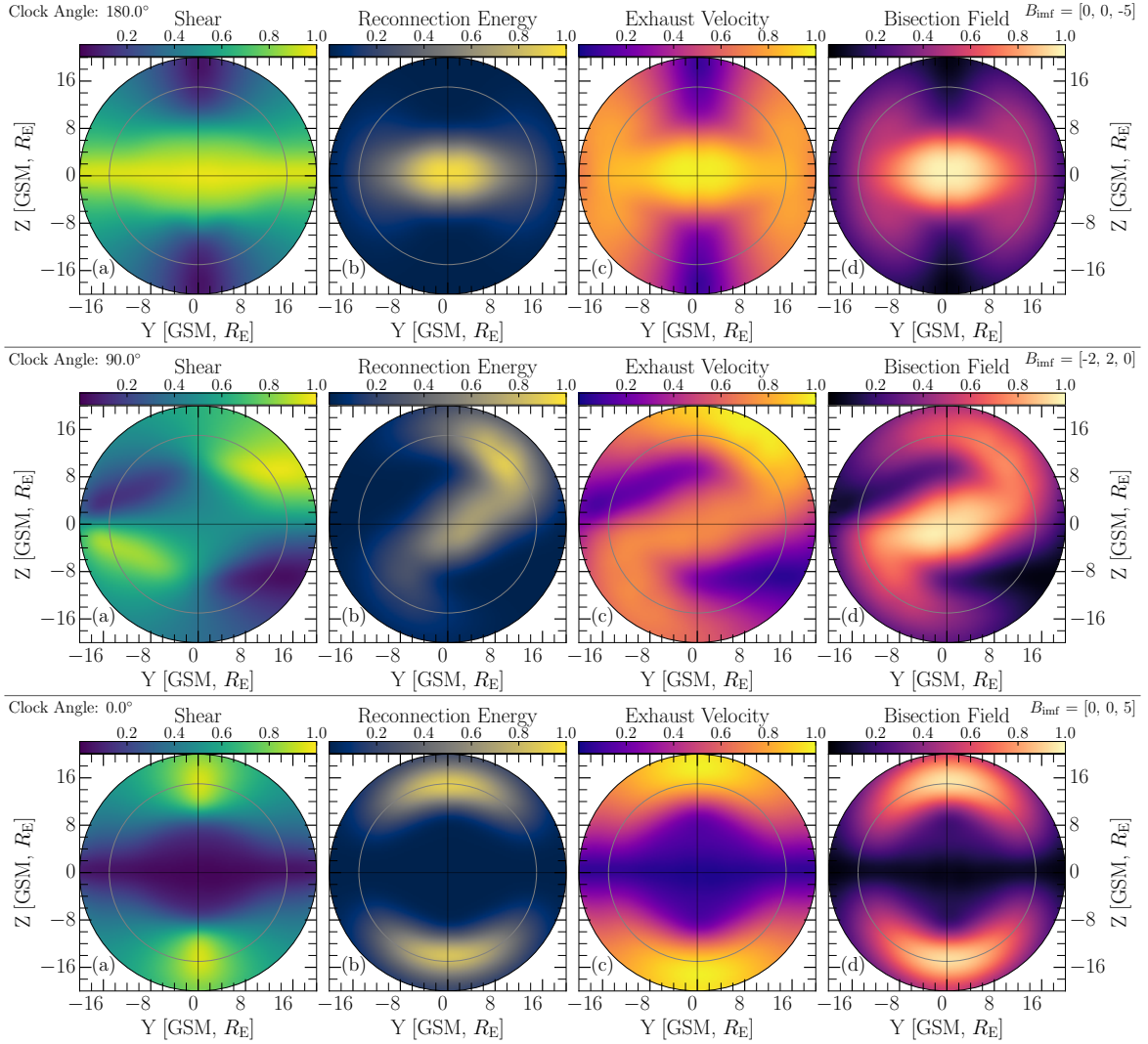

Figure 1. Sample figure of distribution of four parameters discussed in Section 2, projected on the yz-plane. Three rows correspond to three different IMF conditions (from top to bottom, purely southward IMF, Parker spiral and purely northward IMF) shown in the top right corner of each panel. For simplicity, Earth's dipole tilt is assumed to be zero.

3 Data Selection and Methodology

3.1 Data

This investigation uses high resolution OMNI data (1 minute resolution) propagated to the nose of Earth's bow shock (King & Papitashvili, 2005) along with data from the Fast Plasma Instrument (FPI) (Pollock et al., 2016) and the Fluxgate Magnetometer (FGM) (Russell et al., 2016; Torbert et al., 2016) aboard the MMS spacecraft. Since MMS is a constellation of 4 spacecraft, we looked into differences in the output of the model while using data from different spacecraft. We observed that using data from one versus other spacecraft made insignificant changes to the overall result of this study, and thus decided to use data from MMS 3 for this study. For easy identification of jet reversal (see Section 3.2 for more details), the study uses high resolution burst data from FPI which gives a full space density measurement every 150 ms (for ions). Section 3.2 describes how each of these data were used in this study and the methodology in greater detail.

3.2 Methodology

With the MMS spacecraft, between September 2015 and April 2018, 16,782 magnetopause current sheet crossings have been identified and documented (see Paschmann et al. (2018); Haaland et al. (2020) for details of methodology used for identification and classification). A spacecraft crossing the magnetopause current sheet can observe enhanced ion velocity tangential to the current sheet. This enhancement, known as a reconnection jet, is an indication that reconnection is occurring nearby. Enhanced ion-velocities with switching directions are called jet reversals, and are evidence of an X-line nearby the spacecraft position (e.g., Paschmann et al., 1979; Cowley, 1982; Gosling et al., 1982; Pu et al., 2007; Dunlop et al., 2011; Trattner, Burch, et al., 2017; Petrinec et al., 2022).

For each identified crossing, we record a 10-minute long time series centered at the crossing time (t_{cross}). We transform the magnetic field and the ion-velocity from GSM-coordinate (Geocentric Solar Magnetic) to a local LMN-coordinate (boundary-normal) system using the empirical magnetopause model described in Shue et al. (1998). In the code, this was implement using coordinate transformation tools available in PySPEDAS (Grimes et al., 2019). Using the ion properties (density, temperature and energy spectra) we identify the magnetosheath and magnetopause locations. If there are multiple crossings within the 10-minute time period, then the values during the longest interval for both locations are averaged over to get a representative value of each parameter in that region. In the next step, we identify if a jet reversal was observed by MMS during the crossing by inspecting the ion velocity directions. In order to minimize the impact of varying condition of magnetosheath because of changes in the upstream solar wind condition, we subtract the representative ion-velocity, $\langle V_{\text{L}} \rangle$ of magnetosheath from the velocity time series and call the resultant parameter ΔV_{L}, defined as:

$$\Delta V_{\text{L}} = V_{\text{L}} - \langle V_{\text{L,sheath}} \rangle \tag{5}$$

where, $\langle V_{\text{L,sheath}} \rangle$ is the average value of L-component of ion-velocity in the longest magnetosheath interval in the 10-minute period and V_{L} is the time series data of L-component of ion-velocity. We use this velocity, ΔV_{L}, to check for the presence of jet-reversal during crossings. In order to identify jet-reversal, we look for switches in ΔV_{L} by more than $\pm 70 \, \text{km/s}$ within a 2-minute window of the 10-minute time series data. Previous studies (Trattner, Burch, et al., 2017; Petrinec et al., 2022) have used the same velocity change and time window values for a similar dataset. This study adds additional conditions to the crossings in order to constrain uncertain crossing measurements. To remove artificial peaks, the algorithm only identifies a velocity switch as a jet-reversal if ΔV_{L} is larger (and smaller) than $+70 \, \text{km/s}$ (- 70 km/s) continuously for at least a time interval of 3 seconds. Once we find such a time interval, we check if the maximum and minimum val-

239   ues of ΔV_{L} occurred within a 2 minute time interval of each other. Once that condition
240   has been satisfied, we assign time of the jet (t_{jet}) as the time between the maximum and
241   minimum value of ΔV_{L}. If there are multiple instances of $|\Delta V_{\mathrm{L}}| > 70\,\mathrm{km/s}$ within the
242   10 minute period, then the interval which has the highest peak of ΔV_{L} is checked for pres-
243   ence of a jet. The methodology to identify jet reversals is based on methodology devel-
244   oped by Trattner, Burch, et al. (2017) and used in previous statistical studies Trattner,
245   Burch, et al. (2017); Petrinec et al. (2022).

246   Figure 2 shows a typical MMS time series data of the parameters used in this study.
247   The top panel (panel a) shows the ion energy spectra, and the next panel shows the mag-
248   netic field strength in the local LMN-coordinate system. Panel (c) and (d) show the ion-
249   density and parallel and perpendicular temperatures respectively. The dip in ion-density
250   and the corresponding enhancement of ion-temperature around 16:50:30 UTC, along with
251   the change in ion-density spectra, is the indication of spacecraft moving from magnetosheath
252   to magnetosphere. Next, panel (e) show the time series of ion-velocity components. Ver-
253   tical red and blue lines mark the location of reference magnetosphere and magnetosheath,
254   as identified by the automated code described earlier. The last panel (f) shows ΔV_{L}, which
255   is the difference between V_{L} and the average value of V_{L} in the magnetosheath, described
256   by Equation (5). The green vertical line shows the location of the center of the jet, which
257   is at the center point between the maximum and minimum value of ΔV_{L}. The timestamp
258   corresponding to this center point is referred as the time of the jet, t_{jet}.

259   Once a jet has been identified, a 10-minute average value of solar wind observations
260   from OMNI data centered at t_{jet} are used for the upstream condition. These solar wind
261   upstream conditions are then used as input for the Shue-98 (Shue et al., 1998) model to
262   compute the stand-off distance of the magnetopause sub-solar point and the general shape
263   of the magnetopause. The upstream solar wind conditions are then used with the out-
264   put of Shue-98 model as input for Tsyganenko-96 (Tsyganenko, 1996) model, which pro-
265   vides the magnetic field at the magnetopause.

266   For the magnetosheath fields, we use the Cooling-01 (Cooling et al., 2001) model
267   to obtain the draped magnetosheath field just outside the magnetopause. For the Cooling-
268   01 model, the magnetosheath density is derived from MMS data (using the average ob-
269   served value, as previously described) and for the magnetopause ion density we assume
270   a standard density of $0.1\mathrm{cm}^{-3}$. The output from these models is used to compute the
271   value of four parameters (magnetic shear, reconnection energy, exhaust velocity and bi-
272   section field) over the magnetopause spread over a circular region of radius $20\,\mathrm{R_E}$ as de-
273   scribed by Equations (1) to (4).

274   Next, to trace the location of the predicted reconnection line from each model, max-
275   imization of each of the respective parameter (except for Maximum Bisection Model, see
276   Section 2.4) is carried out over the projected circular region along the draped field lines.
277   Thereafter, we compute the minimum 3-D distance of MMS spacecraft from each of the
278   predicted line positions and store the value of distance to make statistical observations.
279   Figure 3 shows the flowchart of the algorithm described above. Figure 4 shows a typ-
280   ical case where we have plotted each of the four parameters on the $yz-plane$ along the
281   magnetopause. The panels from a to d show shear, reconnection energy, exhaust veloc-
282   ity and bisection field. Each of these parameters are normalized against their maximum
283   value in the plane so that they all range from 0 to 1. The grey circle at about $15\,R_{\mathrm{E}}$ cor-
284   responds to the terminator. MMS is represented by the white encircled plus. The red
285   and blue arrow in each panel show the direction of the local magnetosheath field and ion-
286   velocity at the position of MMS. R_{rc} is the measured minimum 3-D distance between
287   the reconnection line and the spacecraft. For this study, cases where the point of min-
288   imum distance was outside the terminator were not used for the statistics.
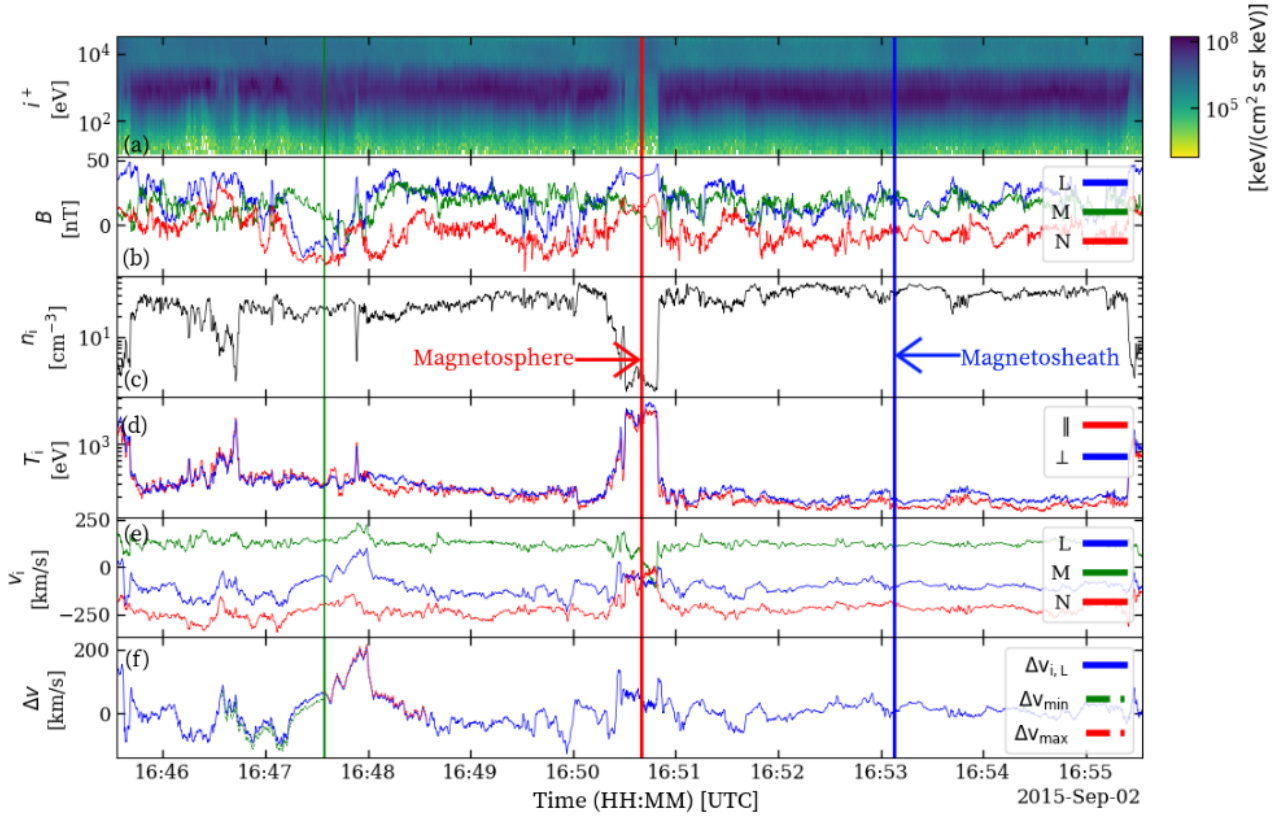
Figure 2. Time series of various data from MMS spacecraft. Top panel shows the ion energy spectra whereas the next panel (panel b) shows the time series of three magnetic field components in LMN-coordinate system. Panel c and d show the ion density and temperatures. Panel e shows the ion-velocity components. Vertical red and blue lines mark the location of magnetosphere and magnetosheath, as identified by the automated code. The last panel shows ΔV_L, which is the difference between V_L and the average value of V_L in the magnetosheath. The green vertical line shows the location of a jet, which is at the center point between the maximum and minimum value of ΔV_L.

4 Results and Discussions

Using the methodology described in Section 3.2, between September 2015 and April 2018, a total of 274 jet reversals were identified. For each of these events we computed the distance between the predicted X-line location and the MMS spacecraft. Figure 5 shows the location of each of the jets in $xy-$ and $yz-$plane with a nominal magnetopause location shown by the dashed-blue line. The two colors represent jet-reversal detection corresponding to the directions of B_z (southward for green and northward for orange). The average value of various solar wind parameters corresponding to the time of observation of each event are listed in Table 2. These values are very similar to nominal solar wind conditions observed at 1 AU by the WIND spacecraft (Wilson III et al., 2021). However, though the nominal value of B_z in the solar wind on average is very close to

```
┌─────────────────────┐                          ┌─────────────────┐          ┌──────────────────┐
│ Magnetopuase current│ 10 minute time series    │ Find location of│          │ Convert B and V to│
│ sheet crossing time ├─────────────────────────▶│ magnetopause and├─────────▶│ LMN coordinate system│
│    $t_{cross}$      │ data centered at $T_{crossing}$ │ magnetosheath│          │                  │
└─────────────────────┘                          └─────────────────┘          └──────────────────┘
```

Figure flowchart:

- **Magnetopuase current sheet crossing time t_{cross}** →(10 minute time series data centered at T_{crossing})→ **Find location of magnetopause and magnetosheath** → **Convert B and V to LMN coordinate system**

- **Compute $\Delta V_{\mathrm{L}} = V_{\mathrm{L}} - < V_{\mathrm{L,\,sheath}} >$**
  - $|\Delta V_{\mathrm{L}}| < 70\,\mathrm{km/s}$ → **No Jet Ignore the crossing**
  - $|\Delta V_{\mathrm{L}}| > 70\,\mathrm{km/s}$ → **Check if $|\Delta V_{\mathrm{L}}| > 70\,\mathrm{km/s}$ for at least 3 seconds**
    - No → **No Jet Ignore the crossing**
    - Yes → **Find the jet time, t_{jet} (time between the maximum and minimum value of ΔV_{L})**

- **Find upstream solar wind conditions corresponding to t_{jet}** → **Run Shue-98, Tsyganenko-96 and Cooling-01 model to get Magnetopause and Magnetosheath fields** →(Compute)→ **1. Magnetic Shear 2. Reconnection Energy 3. Exhaust Velocity 4. Bisection Field** → **Draw X-line for each model by maximizing each parameter** → **Measure minimum distance from each X-line to MMS**
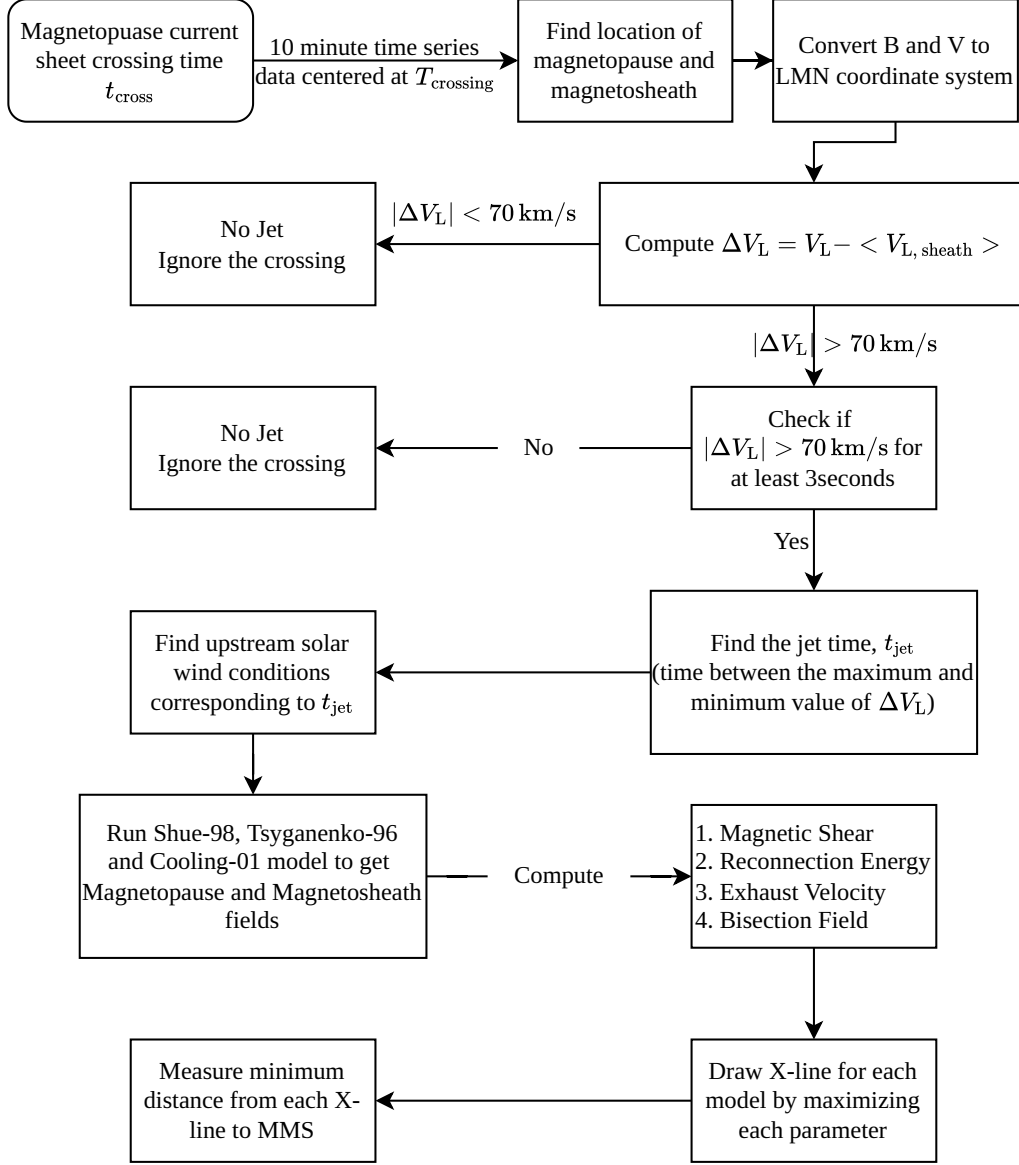
Figure 3. Flowchart of the algorithm used to select MMS magnetopause crossings for jet reversals and comparison to model X-line positions. See text for definition of each term and more details

zero, for the 274 jet reversals observed, the average value of B_{z} in the solar wind was close to -1, which shows a bias of jet reversal detection during southward IMF. This is to be expected because reconnection near the sub-solar region is more common during southward IMF. Statistically, we found that we were twice as likely to find a jet-reversal during southward IMF compared to northward IMF. Figure 6 shows a histogram of the distance of the modeled reconnection X-line (R_{rc}) from the MMS spacecraft. The distance is plotted along the x-axis in the units of Earth radius (R_{E}), with the frequency of events along y-axis. The dashed line in each panel corresponds to the mean value of the histogram.

The performance of the models across the various solar wind conditions are now compared. The average value of distance between spacecraft and the predicted X-line

Table 2. Average values of solar wind parameters during observed jet reversals

Parameter	Percentile		
	5th	50th	95th
$|\mathbf{B}|$ [nT]	2.69	4.76	9.67
n_i [cm^{-3}]	2.22	4.97	12.02
P_{dyn} [nPa]	1.23	2.23	4.88
V_i [km/s]	337	507	693
T_i [ev]	2.55	10.20	27.89

for Maximum Bisection Field Model and Maximum Reconnection Energy Model are similar, though the Maximum Bisection Field Model with an average measured distance of $4.22\,R_{\text{E}}$ gives the lowest value among the four tested models. The histogram for Maximum Bisection Field Model also has the least spread, implying the precision of the model, however it seems to lack the accuracy of the Maximum Shear Model under some conditions (discussed later). The precision of the Maximum Bisection Field Model can be explained, in part, by the inherent observational bias in the data. Most of the jet-reversals were observed by MMS in the equatorial plane, very close to the sub-solar point (see Figure 5). In addition, for most upstream conditions (except for conditions with positive B_{x}), the Maximum Bisection Field Model tends to predict the X-line location along or close to the equator; it therefore makes sense that the spread for this model will be least compared to other models.

Under the condition $B_{\text{z}} < 0$, the accuracy of each model improves compared to all IMF conditions. Figure 7 shows the histogram corresponding to this condition and Table 3 shows the difference in average values corresponding to two different conditions ($B_{\text{z}} > 0$ and $B_{\text{z}} < 0$) along with the average value of measured reconnection distance for each model for three different conditions. The improvement is most significant in the case of Maximum Reconnection Energy Model where the average value changes by $3.15\,R_{\text{E}}$ followed by Maximum Exhaust Velocity Model (a change of $2.53\,R_{\text{E}}$). The correlation between the model accuracy and the value of B_{z} can also be seen in Figure 8. Figure 8 shows the highest value of Pearson correlation coefficient for Maximum Reconnection Energy Model and Maximum Exhaust Velocity Model implying greater dependency of the accuracy of these two models on B_{z} followed by Maximum Shear Model and Maximum Bisection Field Model , which understandably shows the least correlation between the two parameters. For Figure 8, the histogram along each axis shows the distribution of the associated parameter.

Figure 9 shows the distribution between the cone angle ($\theta_{\text{cone}} = \cos^{-1}\left(B_{\text{x}}/|\mathbf{B}|\right)$) and the z-component of IMF. Low θ_{cone} means the IMF is dominated by the radial magnetic field component and likely has a foreshock upstream of the dayside magnetopause. Each bubble represents an observation point and its radius is proportional to the measured distance between X-line and MMS for the corresponding model. The larger bubble implies lesser accuracy in predicting the location of X-line by the model. For both the Maximum Bisection Field Model and Maximum Reconnection Energy Model at $B_{\text{z}} > 0$ there is a visible increment in R_{rc} values (see Table 3). At all θ_{cone}, as long as B_{z} is negative, the two models remain fairly accurate. For mid range values of θ_{cone} (values between [50, 120] degrees), even when B_{z} is positive, the model (Maximum Bisection Field Model and Maximum Reconnection Energy Model) predictions remain accurate. The

Maximum Shear Model behaves in a very similar way with two interesting differences. For mid range values of cone angle, for all values of B_z and especially for positive values, the Maximum Shear Model does the best job of predicting the correct location of X-line. And at low values of cone angle, Maximum Shear Model performs as well as the Maximum Reconnection Energy and Maximum Bisection Field Model. At very high values of θ_{cone} (> 150 degrees) irrespective of the sign of B_z, Maximum Shear Model performs relatively poorly ($\langle R_{\text{c,shear}} \rangle = 9.50 \, R_{\text{E}}$ vs $\langle R_{\text{c,bisec}} \rangle = 3.65 \, R_{\text{E}}$).

In Figure 9 there is also an asymmetry in the computed values of R_{rc} for very low ($\theta_{\text{cone}} < 30$ degrees) and very high ($\theta_{\text{cone}} > 150$ degrees) cone angles for all models. This can in part be explained the fact that the effect on the draping filed, as computed using Cooling-01 model, is not symmetric for positive and negative B_x. Also, while computing the fields using T-96 model, dipole tilt of the Earth is considered whereas it is ignored during computation of draping field using Cooling-01 model. This also leads to some asymmetry to the result of computed distance. Though this asymmetry is present in all cases, it is most pronounced for Maximum Shear Model. Previous work has reported the Maximum Shear Model struggled during time periods with large B_x or small θ_{cone} possibly due to the draping model being used (Trattner, Thresher, et al., 2017).

In order to look at the affect of B_y on the accuracy of the models, we plot $B_y/|\mathbf{B}|$ against the z-component of IMF in Figure 10. Figure 10 is made in a similar style to that of figure Figure 9, except $B_y/|\mathbf{B}|$ is along the y-axis. We plot this ratio instead of the value of B_y in order to look at the variation in different X-line predictions based on how dominant the y-component is. It has been noted in literature (Trattner, Thresher, et al., 2017) that for dominant B_y the Maximum Shear Model still works even for a northward IMF. We see that to be the case here as well in the top left panel of Figure 10 corresponding to the Maximum Shear Model. For other models shown in Figure 10 the effects of B_y are much less prominent. This is clear from Table 4 where we have shown the average values of R_c corresponding to cases $B_y/|\mathbf{B}| > 0.7$ and $B_y/|\mathbf{B}| < 0.3$ as well as percentage change in the average values for all four models. Maximum Shear Model has the highest change percentage whereas Maximum Bisection Field Model is least affected by the change in $B_y/|\mathbf{B}|$. The effect of B_y is even more dominant when we only consider the cases where the IMF was northward. In such conditions, the accuracy of Maximum Shear Model increases by $\sim 45\%$.

The Maximum Exhaust Velocity Model performs worst compared to all the other models in this study. Although there is significant improvement in prediction accuracy when we consider cases of only negative B_z (see Table 3), the average R_{rc} values are more than all other models. Part of the reason for this poor performance might be the fact that the Maximum Exhaust Velocity Model uses both the magnetic field and density of ions in its computation of the hybrid Alfvén speed. We explicitly assume the value of ion density in the magnetosphere as $0.1 \, cm^{-3}$ which would have the impact on the accuracy of the computed velocity.

5 Summary and Conclusion

Magnetic reconnection occurring at the magnetopause of Earth is known to exert a significant influence on magnetospheric convection and facilitates the influx of mass and energy into the magnetosphere/ionosphere system. Despite its importance, the factors governing the location of a dayside magnetic reconnecting X-line are not well understood. Several models have been proposed to predict the location of the X-line. For this study, we chose to compare the statistical performance of four such models. These models share a common assumption that the X-line location can be determined by the maximization of a physical quantity along the magnetopause boundary. The models considered maximizes the magnetic shear, magnetic reconnection energy, hybrid exhaust velocity and the bisection field. We referred to them as Maximum Shear Model, Maximum

Table 3.   Table of average distance between MMS observation and model predicted X-line locations for different conditions of z-component of IMF B_z. $\langle R_{c,B_z<0} \rangle$ refers to average distance from reconnection line for cases where $B_Z < 0$.

Model	Average Distance (R_{rc})			Difference, ΔR_{rc}
	All IMF conditions	$\langle R_{rc,B_z<0} \rangle$	$\langle R_{rc,B_z>0} \rangle$	$(\langle R_{rc,B_z>0} \rangle - \langle R_{rc,B_z<0} \rangle)$
Maximum Shear Model	5.16	4.53	6.34	1.81
Maximum Reconnection Energy Model	4.65	3.74	6.88	3.14
Maximum Exhaust Velocity Model	5.93	5.16	7.69	2.53
Maximum Bisection Field Model	4.22	3.65	5.27	1.62

Table 4.   Table of average distance between MMS observation and model predicted X-line locations for different values of IMF $B_y/|\mathbf{B}|$

Model	Average Distance (R_E)		Difference, ΔR_{rc}
	$B_y/|\mathbf{B}| < 0.3$	$B_y/|\mathbf{B}| > 0.8$	(Percentage)
Maximum Shear Model	7.57	5.48	27.61
Maximum Reconnection Energy Model	6.79	5.45	19.73
Maximum Exhaust Velocity Model	8.98	7.95	11.47
Maximum Bisection Field Model	4.82	4.69	2.70

Reconnection Energy Model, Maximum Exhaust Velocity Model, and Maximum Bisection Field Model.

We report the performance of these models under various upstream solar wind conditions. We used high cadence MMS data in conjunction with data from OMNI. Output from models (Tsyganenko-96, Shue-98 and Cooling-01) were used to get the magnetospheric and magnetosheath magnetic fields. In order to locate the actual locations of the X-line, we found the time intervals where MMS observed jet reversals with sustained high positive and negative values of ion velocities for at least 3 seconds in each direction, within a 2 minute window. The location of MMS at these intervals were then compared with the prediction for an X-line from the aforementioned four different models. We computed the shortest distance between the predicted X-line and the MMS location. For the 274 jet reversals observed between September 2015 and April 2018, under no constraints on the upstream IMF conditions, the Maximum Bisection Field Model gives the shortest average distance from the estimated X-line compared to the other models with an average value of $R_{rc} = 4.22\,R_{E}$. The Maximum Reconnection Energy Model does a comparable job with an average value of $R_{rc} = 4.65\,R_{E}$. For the cases where $B_z < 0$, we observe maximum improvement for the Maximum Reconnection Energy ($R_{rc} = 3.74\,R_{E}$) thereby implying strongest dependence on B_z. Though for Maximum Bisection Field Model, the improvement is not as significant ($R_{rc} = 3.65\,R_{E}$), it still is the best model. Under all circumstances, we found that the Maximum Bisection Model performed best.

Considering the effect of B_y, we reconfirmed the results of (Trattner, Thresher, et al., 2017), that for a dominant B_y, ($B_y/|\mathbf{B}| > 0.8$), the Maximum Shear Model performs well, at par with the Maximum Reconnection Energy Model and slightly worse than the Maximum Bisection Field Model. The difference in the improvement of the Maximum Shear Model was highest ($\sim 28\%$) for the four tested models. If we consider dominant B_y along with $B_z > 0$, the improvement in the model increases to $\sim 45\%$.

Overall, the Maximum Bisection Field Model seems to perform best for different upstream conditions and also appears to be most precise. However, part of the reason can be attributed to the inherent observational bias in the MMS data. The Maximum Bisection Field Model tends to predict the location of X-line along or close to the equator, which is also where MMS observed most of the jet reversals (see Figure 5).

Among the four models we compared and various solar wind conditions that we observed, the Maximum Exhaust Velocity Model seems to perform poorest. This can party be because in this study we assumed the magnetospheric ion density to be constant ($n_i = 0.1\,cm^{-3}$) which is not necessarily true. An accurate measurement of the density would alter the hybrid Alfvén velocity and thus affect the average values of measured distance.

Though, as expected, the accuracy of all the models improves with the strength of southwards IMF, the effect is most pronounced for Maximum Exhaust Velocity Model and and least for the Maximum Bisection Field Model as seen in Figure 8. The Maximum Exhaust Velocity Model is also most affected by the extreme values of the cone angle ($< 30°$ and $> 150°$). Though for small cone angles, and for southward oriented IMF, Maximum Shear Model is fairly accurate, at high values of cone angle, for all B_z, the model tends to perform poorly, as seen in Figure 9. For this condition, however, the Maximum Reconnection Energy and the Maximum Bisection Field Model remain largely unaffected.

References

Cassak, P. A., & Fuselier, S. A. (2016). Reconnection at earth's dayside magnetopause. In *Magnetic reconnection* (pp. 213–276). Springer International Publishing. doi: 10.1007/978-3-319-26432-5_6

Cassak, P. A., & Shay, M. A. (2007, oct). Scaling of asymmetric magnetic reconnection: General theory and collisional simulations. *Physics of Plasmas*, *14*(10), 102114. doi: 10.1063/1.2795630

Cooling, B. M. A., Owen, C. J., & Schwartz, S. J. (2001, sep). Role of the magnetosheath flow in determining the motion of open flux tubes. *Journal of Geophysical Research: Space Physics*, *106*(A9), 18763–18775. doi: 10.1029/2000ja000455

Cowley, S. W. H. (1982). The causes of convection in the earth's magnetosphere: A review of developments during the IMS. *Reviews of Geophysics*, *20*(3), 531. doi: 10.1029/rg020i003p00531

Crooker, N. U. (1979). Dayside merging and cusp geometry. *Journal of Geophysical Research*, *84*(A3), 951. doi: 10.1029/ja084ia03p00951

Dungey, J. W. (1961, jan). Interplanetary magnetic field and the auroral zones. *Physical Review Letters*, *6*(2), 47–48. doi: 10.1103/physrevlett.6.47

Dunlop, M. W., Zhang, Q.-H., Bogdanova, Y. V., Trattner, K. J., Pu, Z., Hasegawa, H., . . . Carr, C. (2011, sep). Magnetopause reconnection across wide local time. *Annales Geophysicae*, *29*(9), 1683–1697. doi: 10.5194/angeo-29-1683-2011

Fuselier, S. A., Lewis, W. S., Schiff, C., Ergun, R., Burch, J. L., Petrinec, S. M., & Trattner, K. J. (2014, sep). Magnetospheric multiscale science mission profile and operations. *Space Science Reviews*, *199*(1-4), 77–103. doi: 10.1007/s11214-014-0087-x

Fuselier, S. A., Trattner, K. J., & Petrinec, S. M. (2011, oct). Antiparallel and component reconnection at the dayside magnetopause. *Journal of Geophysical Research: Space Physics*, *116*(A10), n/a–n/a. doi: 10.1029/2011ja016888

Fuselier, S. A., Vines, S. K., Burch, J. L., Petrinec, S. M., Trattner, K. J., Cassak, P. A., . . . Webster, J. M. (2017, may). Large-scale characteristics of reconnection diffusion regions and associated magnetopause crossings observed by MMS. *Journal of Geophysical Research: Space Physics*, *122*(5), 5466–5486. doi: 10.1002/2017ja024024

Gonzalez, W. D., & Mozer, F. S. (1974, oct). A quantitative model for the potential resulting from reconnection with an arbitrary interplanetary magnetic field. *Journal of Geophysical Research*, *79*(28), 4186–4194. doi: 10.1029/ja079i028p04186

Gosling, J. T., Asbridge, J. R., Bame, S. J., Feldman, W. C., Paschmann, G., Sckopke, N., & Russell, C. T. (1982). Evidence for quasi-stationary reconnection at the dayside magnetopause. *Journal of Geophysical Research*, *87*(A4), 2147. doi: 10.1029/ja087ia04p02147

Grimes, E. W., Hatzigeorgiu, N., Lewis, J. W., Russell, C., McTiernan, J. M., Drozdov, A., & Angelopoulos, V. (2019, December). pySPEDAS: Space Physics Environment Data Analysis Software in Python. In *Agu fall meeting abstracts* (Vol. 2019, p. SH41C-3313).

Haaland, S., Paschmann, G., Øieroset, M., Phan, T., Hasegawa, H., Fuselier, S. A., . . . Burch, J. (2020, March). Characteristics of the Flank Magnetopause: MMS Results. *Journal of Geophysical Research (Space Physics)*, *125*(3), e27623. doi: 10.1029/2019JA027623

Hesse, M., Aunai, N., Zenitani, S., Kuznetsova, M., & Birn, J. (2013, jun). Aspects of collisionless magnetic reconnection in asymmetric systems. *Physics of Plasmas*, *20*(6), 061210. doi: 10.1063/1.4811467

King, J. H., & Papitashvili, N. E. (2005). *Solar wind spatial scales in and comparisons of hourly wind and ace plasma and magnetic field data* (Vol. 110) (No. A2). Retrieved from https://agupubs.onlinelibrary.wiley.com/doi/abs/10.1029/2004JA010649 doi: https://doi.org/10.1029/2004JA010649

Komar, C. M., Fermo, R. L., & Cassak, P. A. (2015, jan). Comparative analysis of dayside magnetic reconnection models in global magnetosphere simula-

tions. *Journal of Geophysical Research: Space Physics*, *120*(1), 276–294. doi: 10.1002/2014ja020587

Liu, Y.-H., Hesse, M., Li, T. C., Kuznetsova, M., & Le, A. (2018, jun). Orientation and stability of asymmetric magnetic reconnection x line. *Journal of Geophysical Research: Space Physics*, *123*(6), 4908–4920. doi: 10.1029/2018ja025410

Moore, T. E. (2002). The dayside reconnection x line. *Journal of Geophysical Research*, *107*(A10). doi: 10.1029/2002ja009381

Muzamil, F. M., Farrugia, C. J., Torbert, R. B., Pritchett, P. R., Mozer, F. S., Scudder, J. D., ... Wilson, L. (2014, sep). Structure of a reconnection layer poleward of the cusp: Extreme density asymmetry and a guide field. *Journal of Geophysical Research: Space Physics*, *119*(9), 7343–7362. doi: 10.1002/2014ja019879

Paschmann, G. (2008, oct). Recent in-situ observations of magnetic reconnection in near-earth space. *Geophysical Research Letters*, *35*(19). doi: 10.1029/2008gl035297

Paschmann, G., Haaland, S. E., Phan, T. D., Sonnerup, B. U. O., Burch, J. L., Torbert, R. B., ... Fuselier, S. A. (2018, mar). *Large-scale survey of the structure of the dayside magnetopause by MMS.* American Geophysical Union (AGU). doi: 10.1002/2017ja025121

Paschmann, G., Øieroset, M., & Phan, T. (2013, feb). In-situ observations of reconnection in space. *Space Science Reviews*, *178*(2-4), 385–417. doi: 10.1007/s11214-012-9957-2

Paschmann, G., Papamastorakis, I., Baumjohann, W., Sckopke, N., Carlson, C. W., Sonnerup, B. U. O., & Lhr, H. (1986). The magnetopause for large magnetic shear: AMPTE/IRM observations. *Journal of Geophysical Research*, *91*(A10), 11099. doi: 10.1029/ja091ia10p11099

Paschmann, G., Sonnerup, B. U. ., Papamastorakis, I., Sckopke, N., Haerendel, G., Bame, S. J., ... Elphic, R. C. (1979, nov). Plasma acceleration at the earth's magnetopause: evidence for reconnection. *Nature*, *282*(5736), 243–246. doi: 10.1038/282243a0

Petrinec, S. M., Burch, J. L., Fuselier, S. A., Trattner, K. J., Giles, B. L., & Strangeway, R. J. (2022, jun). *On the occurrence of magnetic reconnection along the terrestrial magnetopause, using magnetospheric multiscale (MMS) observations in proximity to the reconnection site* (Vol. 127) (No. 6). American Geophysical Union (AGU). Retrieved from https://agupubs.onlinelibrary.wiley.com/doi/abs/10.1029/2021JA029669 (e2021JA029669 2021JA029669) doi: 10.1029/2021ja029669

Pollock, C., Moore, T., Jacques, A., Burch, J., Gliese, U., Saito, Y., ... Zeuch, M. (2016, March). Fast plasma investigation for magnetospheric multiscale. *Space Science Reviews*, *199*, 331-406. doi: 10.1007/s11214-016-0245-4

Pu, Z. Y., Zhang, X. G., Wang, X. G., Wang, J., Zhou, X.-Z., Dunlop, M. W., ... Escoubet, P. (2007, oct). Global view of dayside magnetic reconnection with the dusk-dawn IMF orientation: A statistical study for double star and cluster data. *Geophysical Research Letters*, *34*(20). doi: 10.1029/2007gl030336

Russell, C. T., Anderson, B. J., Baumjohann, W., Bromund, K. R., Dearborn, D., Fischer, D., ... Richter, I. (2016, March). The magnetospheric multiscale magnetometers. *Space Science Reviews*, *199*, 189-256. doi: 10.1007/s11214-014-0057-3

Shue, J.-H., Song, P., Russell, C. T., Steinberg, J. T., Chao, J. K., Zastenker, G., ... Kawano, H. (1998, aug). Magnetopause location under extreme solar wind conditions. *Journal of Geophysical Research: Space Physics*, *103*(A8), 17691–17700. doi: 10.1029/98ja01103

Souza, V. M., Gonzalez, W. D., Sibeck, D. G., Koga, D., Walsh, B. M., & Mendes, O. (2017, apr). Comparative study of three reconnection x line models at the earth's dayside magnetopause using in situ observations. *Journal of Geophysi-*

cal Research: Space Physics, *122*(4), 4228–4250. doi: 10.1002/2016ja023790

Torbert, R. B., Russell, C. T., Magnes, W., Ergun, R. E., Lindqvist, P. A., Le Con-
  tel, O., . . . Lappalainen, K. (2016, March). The FIELDS Instrument Suite on
  MMS: Scientific Objectives, Measurements, and Data Products. *Space Science
  Reviews*, *199*(1-4), 105-135. doi: 10.1007/s11214-014-0109-8

Trattner, K. J., Burch, J. L., Ergun, R., Eriksson, S., Fuselier, S. A., Giles, B. L., . . .
  Wilder, F. D. (2017, dec). The MMS dayside magnetic reconnection locations
  during phase 1 and their relation to the predictions of the maximum mag-
  netic shear model. *Journal of Geophysical Research: Space Physics*, *122*(12),
  11,991–12,005. doi: 10.1002/2017ja024488

Trattner, K. J., Mulcock, J. S., Petrinec, S. M., & Fuselier, S. A. (2007). Prob-
  ing the boundary between antiparallel and component reconnection dur-
  ing southward interplanetary magnetic field conditions. *Journal of Geo-
  physical Research: Space Physics*, *112*(A8). Retrieved from `https://
  agupubs.onlinelibrary.wiley.com/doi/abs/10.1029/2007JA012270` doi:
  https://doi.org/10.1029/2007JA012270

Trattner, K. J., Petrinec, S. M., & Fuselier, S. A. (2021, April). The location
  of magnetic reconnection at earth's magnetopause. *Space Science Re-
  views*, *217*(3), 41. Retrieved from `https://ui.adsabs.harvard.edu/abs/
  2021SSRv..217...41T` doi: 10.1007/s11214-021-00817-8

Trattner, K. J., Thresher, S., Trenchi, L., Fuselier, S. A., Petrinec, S. M., Peter-
  son, W. K., & Marcucci, M. F. (2017, jan). On the occurrence of magnetic
  reconnection equatorward of the cusps at the earth's magnetopause during
  northward IMF conditions. *Journal of Geophysical Research: Space Physics*,
  122(1), 605–617. doi: 10.1002/2016ja023398

Tsyganenko, N. A. (1996, October). Effects of the solar wind conditions in the
  global magnetospheric configurations as deduced from data-based field models
  (invited). In E. J. Rolfe & B. Kaldeich (Eds.), *International conference on sub-
  storms* (Vol. 389, p. 181). Retrieved from `https://ui.adsabs.harvard.edu/
  abs/1996ESASP.389..181T`

Wilson III, L. B., Brosius, A. L., Gopalswamy, N., Nieves-Chinchilla, T., Szabo, A.,
  Hurley, K., . . . TenBarge, J. M. (2021). A quarter century of wind space-
  craft discoveries. *Reviews of Geophysics*, *59*(2), e2020RG000714. Retrieved
  from `https://agupubs.onlinelibrary.wiley.com/doi/abs/10.1029/
  2020RG000714` (e2020RG000714 2020RG000714) doi: https://doi.org/10.1029/
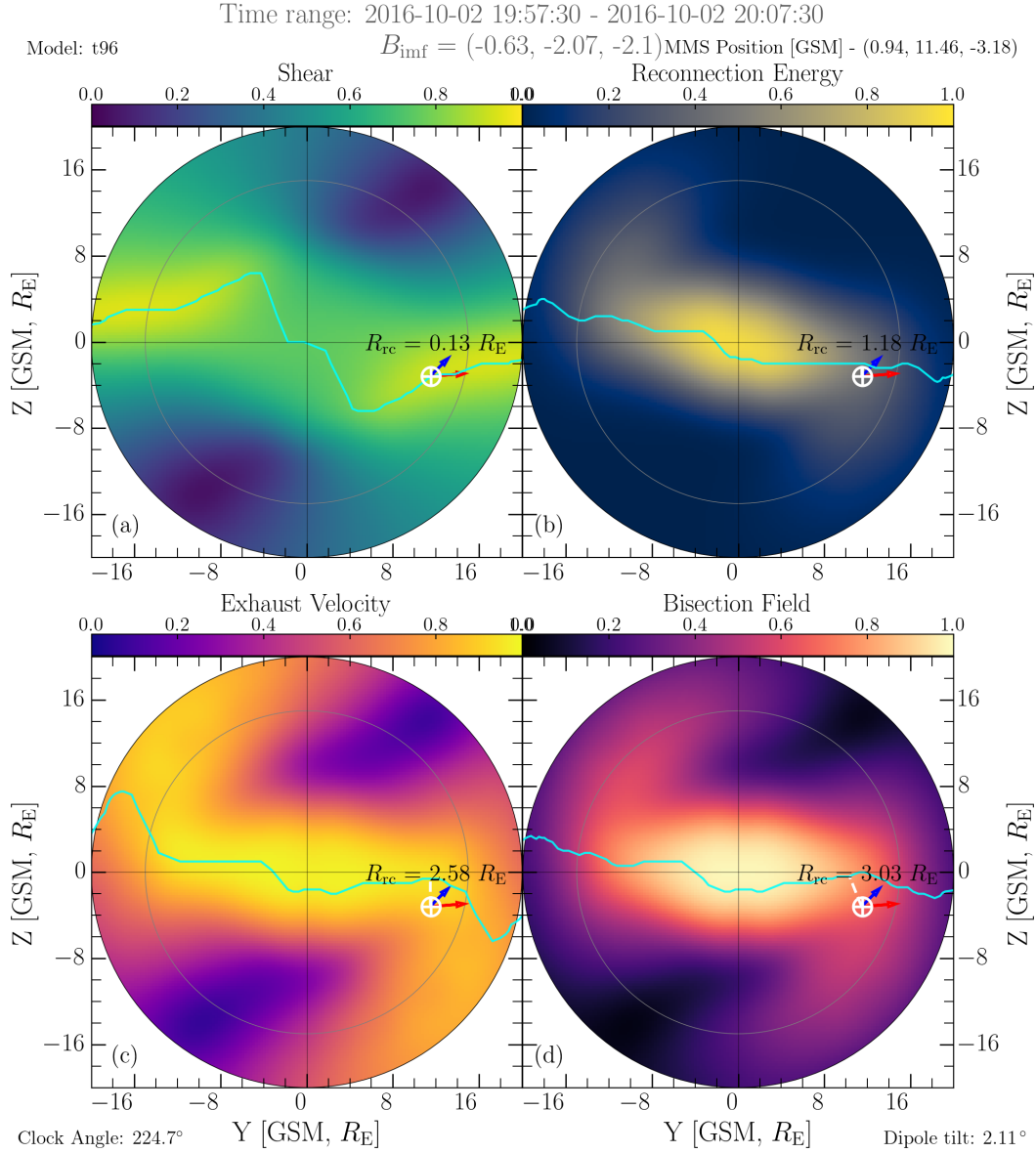 2020RG000714

Figure 4. Location of reconnection line, cyan color, from four different models. MMS is represented by the white encircled plus. Red arrow shows the direction of local magnetosheath field whereas blue arrow shows the direction of local ion-velocity. R_{rc} is the measured minimum distance between the reconnection line and the spacecraft.
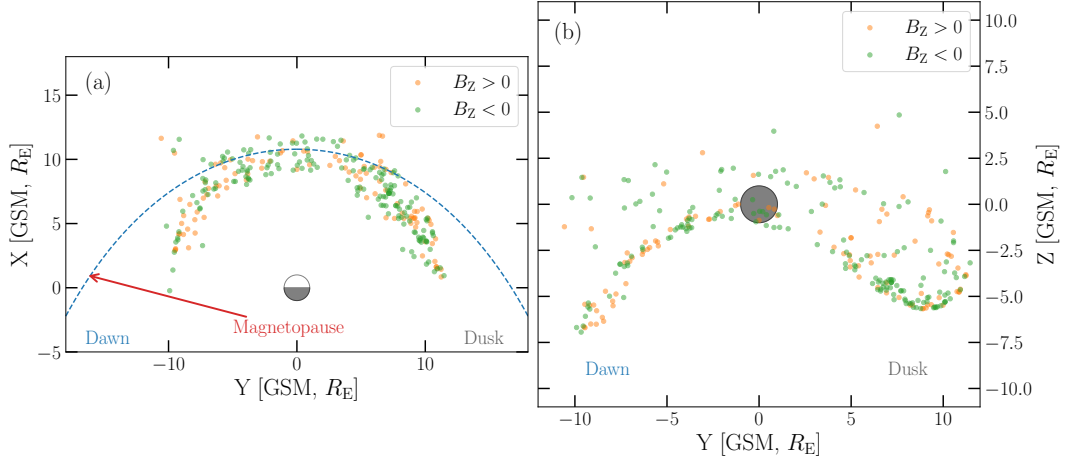
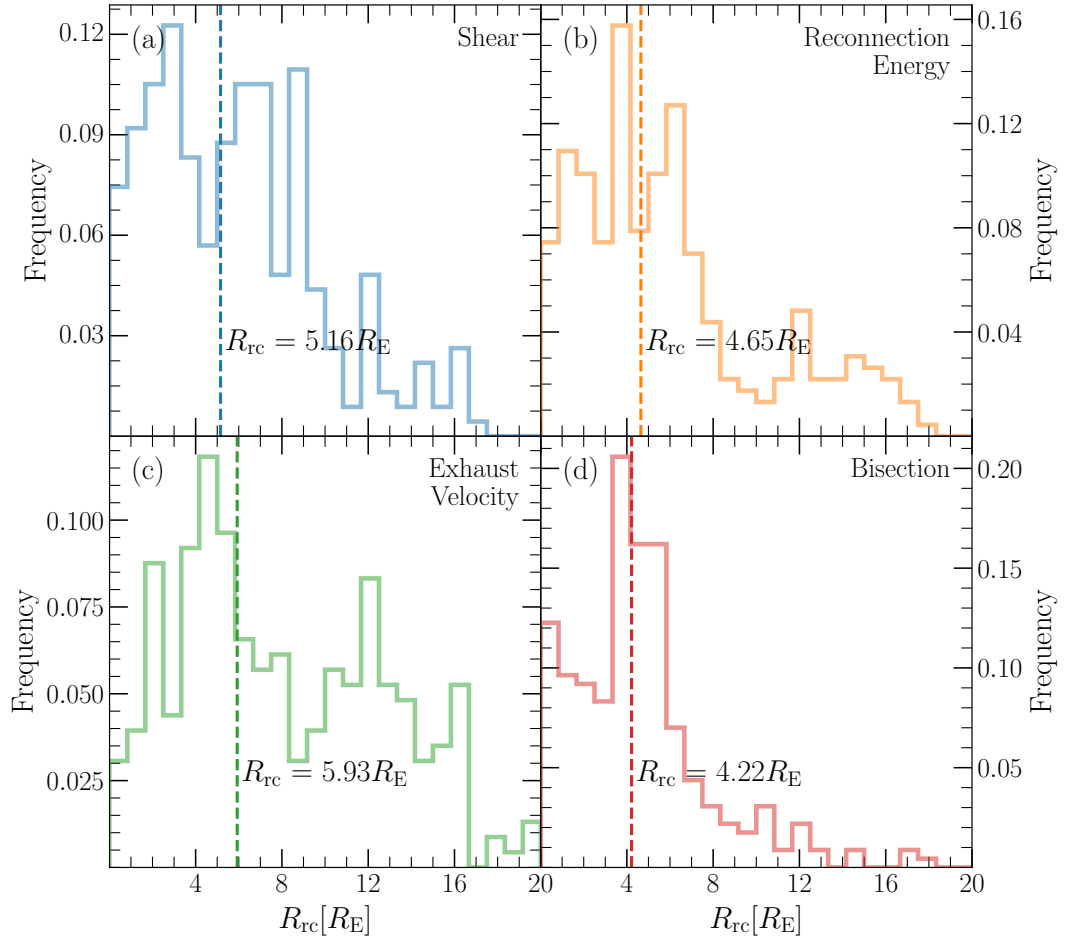**Figure 5.** Location of all the reconnection events used in this study, as observed by MMS, with nominal magnetopause shown as a dashed-blue line.

Figure 6. A histogram of shortest distance between MMS spacecraft and the predicted X-line location by different models. The distance is plotted along x-axis in units of Earth radius, with counts along y-axis. Vertical dashed line in each Panel corresponds to the mean distance of 274 individual measurements.
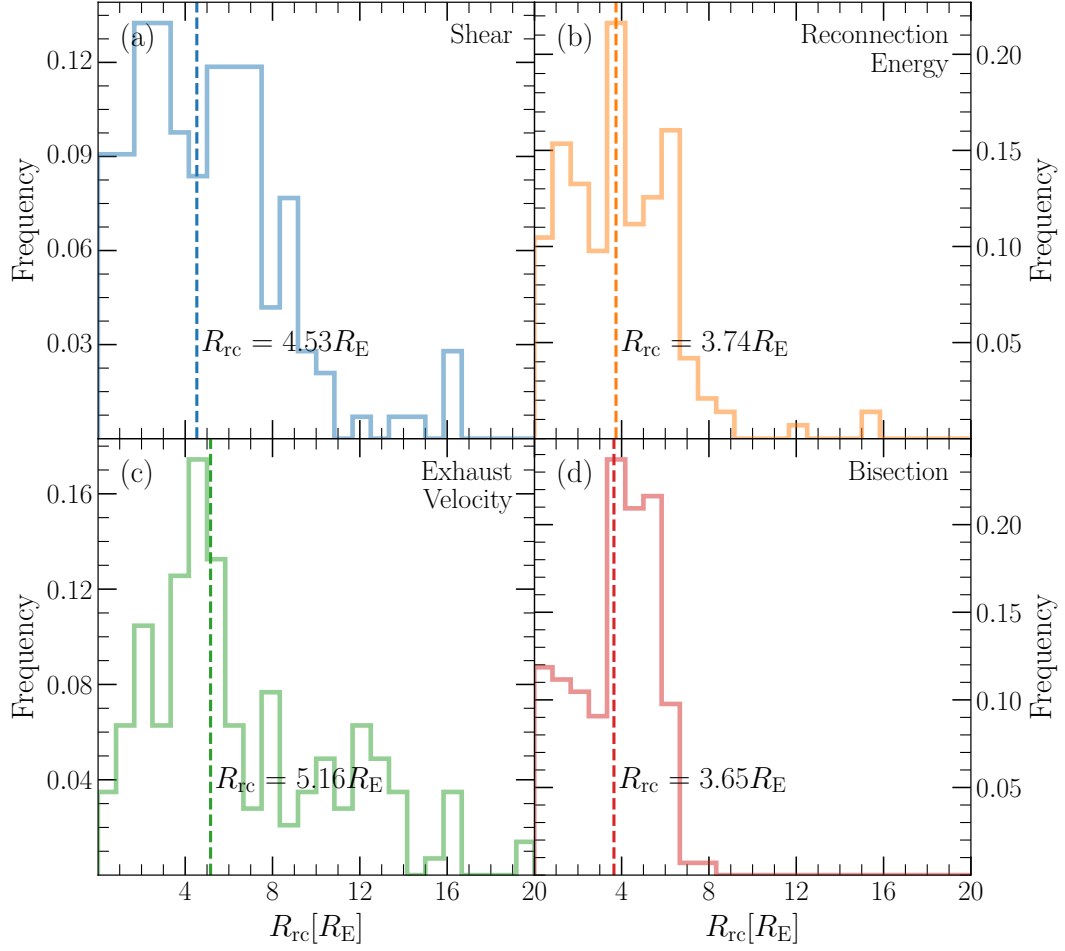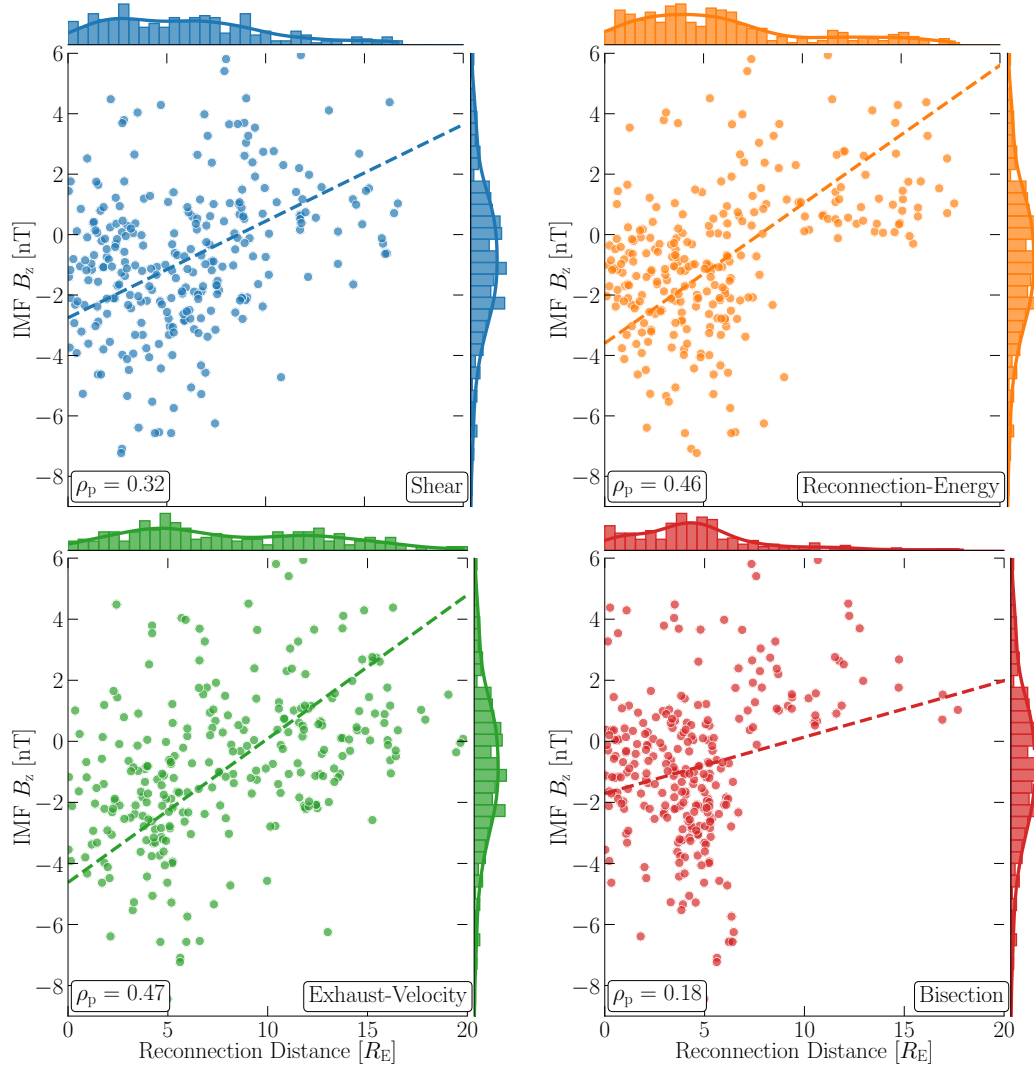
Figure 7. A histogram of shortest distance between MMS spacecraft and the predicted X-line location by different models when $B_z < 0$. The distance is plotted along x-axis in units of Earth radius, with counts along y-axis. Vertical dashed line in each panel corresponds to the mean distance.

Figure 8. Correlation between the z-component of IMF and the distance between the predicted X-line and MMS for different models. ρ_p is the Pearson correlation coefficient. The dashed lined is the trend line with ρ_p as slope. The histogram along the edges shows the distribution of parameters
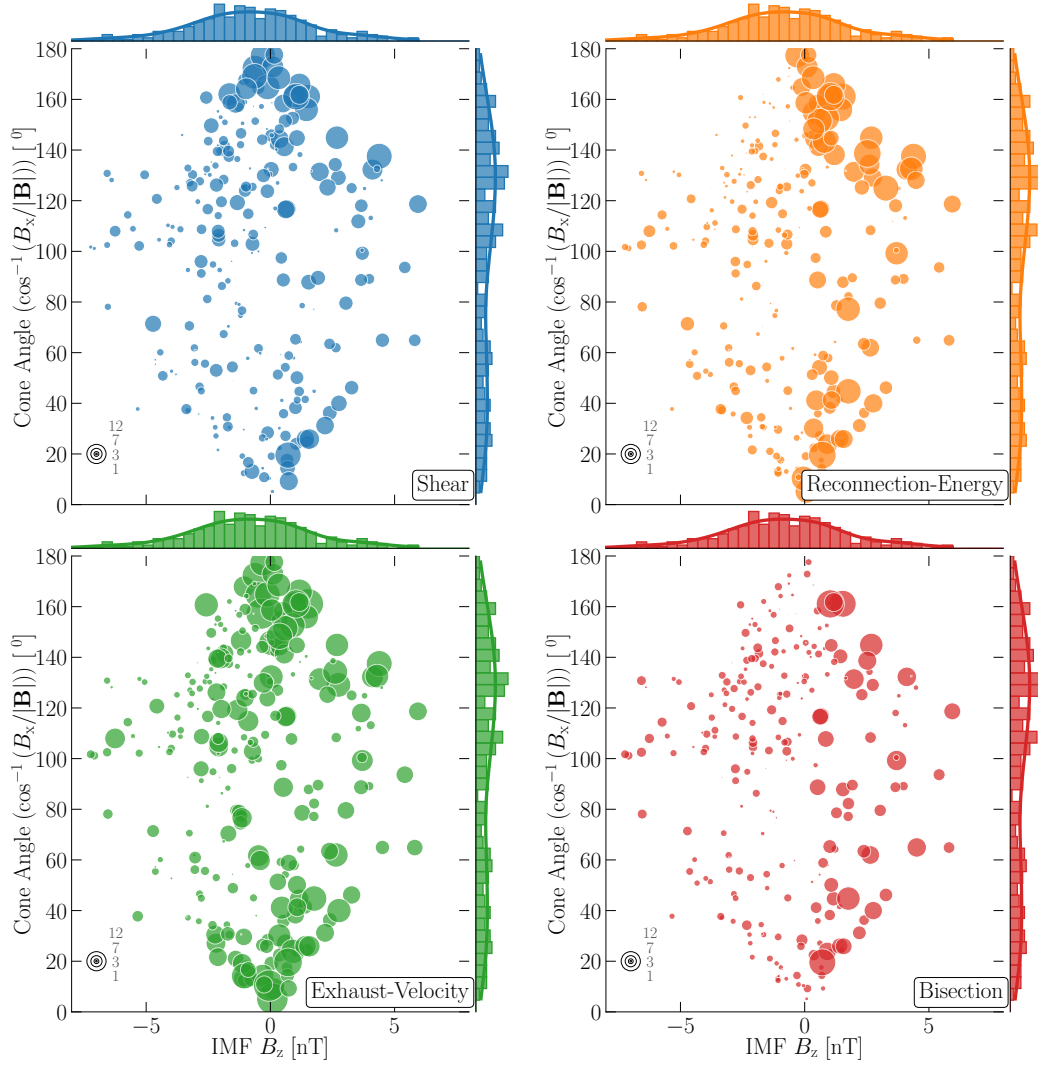
Figure 9. Plot between the IMF cone angle and the corresponding z-component for different models. The size of each circular marker is a representative of measured reconnection distance from the predicted X-line location. Histograms on each of the axis represents the distribution of the parameter along those axes.
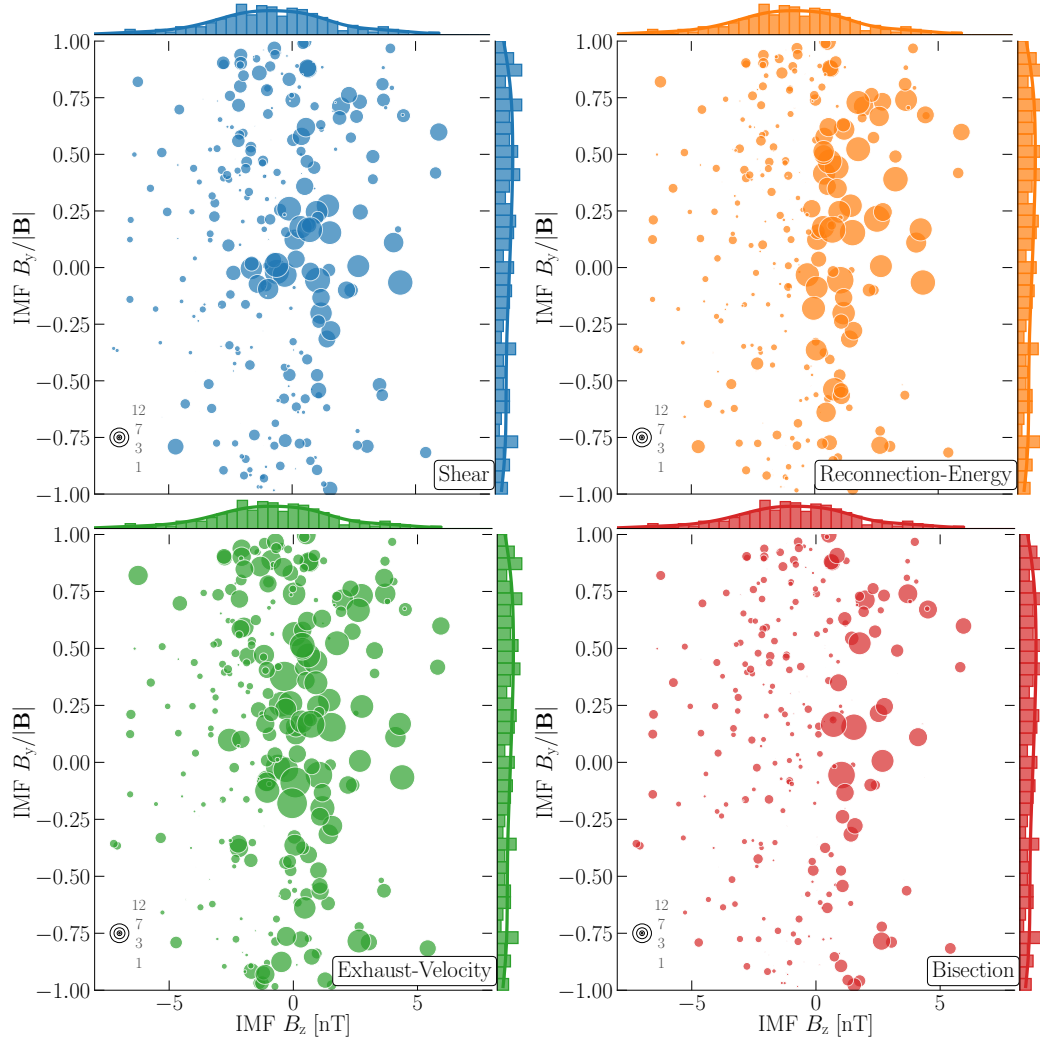
Figure 10. Plot between the ratio of IMF y-component to its magnitude and corresponding z-component for different models. The size of each circular marker is a representative of measured reconnection distance from the predicted X-line location. Histograms on each of the axis represents the distribution of the parameter along those axes